^{6}Li$(p, \gamma)^7$Be reaction rate in the light of the new data of the Laboratory for Underground Nuclear Astrophysics

S. B. Dubovichenko,[1] A. S. Tkachenko,[1] R. Ya. Kezerashvili,[2,3] N. A. Burkova,[4] and A. V. Dzhazairov-Kakhramanov[1,*]

[1]*Fesenkov Astrophysical Institute "NCSRT" ASA MDASI RK, 050020 Almaty, Kazakhstan*
[2]*New York City College of Technology, City University of New York, Brooklyn, New York 11201, USA*
[3]*Graduate School and University Center, City University of New York, New York 10016, USA*
[4]*al-Farabi Kazakh National University, 050040 Almaty, Kazakhstan*

(Received 19 January 2022; revised 1 April 2022; accepted 9 June 2022; published 27 June 2022; corrected 5 July 2022)

We present new calculations of the astrophysical S factor and reaction rate for the ^{6}Li$(p, \gamma)^7$Be reaction at energies of 10 keV to 5 MeV in the framework of a modified potential cluster model with forbidden states, including low lying resonances. The astrophysical $S(E)$ factor is compared with the available experimental data and calculations done within different models. The results for the S factor are in good agreement with the data set (for $E < 0.3$ MeV) and calculations (for $E < 0.6$ MeV) of the LUNA Collaboration [Phys. Rev. C **102**, 052802(R) (2020)]. The recommended extrapolated zero value $S(0)$ turned out to be 101 eV b. Using the theoretical total cross sections, the ^{6}Li$(p, \gamma)^7$Be capture reaction rate is calculated at temperatures ranging from $0.01T_9$ to $10T_9$ and compared with NACRE and NACRE II. Analytical expressions for the S factor and reaction rate are given, and the effect of low-lying resonances on the reaction rate is estimated. We suggest updating the NACRE and NACRE II databases in light of the new LUNA data and present calculations.

DOI: 10.1103/PhysRevC.105.065806

I. INTRODUCTION

The radiative ^{6}Li$(p, \gamma)^7$Be capture reaction is of great interest in nuclear astrophysics [1,2]. In particular, the long-standing cosmological lithium problem stems from the remarkable discrepancy between astronomical observations of primordial lithium abundances and theoretical predictions [3]. The standard model of the Big Bang overpredicts the measured primordial abundance of the lithium isotope ^{7}Li. To produce ^{7}Li, ^{7}Be plays a pivotal role in the big-bang nucleosynthesis. The reaction ^{6}Li$(p, \gamma)^7$Be plays an important role in the consumption of ^{6}Li and formation of ^{7}Be. At the end of big-bang nucleosynthesis ^{7}Be will eventually decay into ^{7}Li [4,5]. Since 1955 the ^{6}Li$(p, \gamma)^7$Be reaction at low energies has been studied by several experimental groups [6–14]. Measurements of the astrophysical S factor of this reaction were limited to the energy range of 35 keV to 1.2 MeV. The astrophysical S factor and reaction rate of the ^{6}Li$(p, \gamma)^7$Be process were studied in the framework of different theoretical approaches and methods [4,14–20]. A detailed review of the theoretical and experimental current status is given in Ref. [12].

In 2020, new experimental data were obtained in the Laboratory for Underground Nuclear Astrophysics (LUNA) [12], and they excluded the possibility of resonance mentioned in [11]. It seems challenging to consider this reaction in the astrophysical energy range, for which experimental data are available. In particular, our interest is the reexamination of S factor and has two foci: (i) to consider ^{6}Li$(p, \gamma)^7$Be within the framework of the modified potential cluster model (MPCM) with the classification of bound and scattering states according to Young's orbital diagrams [21]; (ii) to describe the S factor using all available experimental data and to obtain the reaction rate. While assessing the reliability of MPCM, it is reasonable to extend the energy interval up to 5 MeV to estimate the role of resonances in this energy range.

In this paper, we investigate the energy dependence of the astrophysical S factor of the ^{6}Li$(p, \gamma)^7$Be reaction at energies of 10 keV to 5 MeV. By considering several resonances, including a wide resonance at $E_x = 9.9$ MeV, the reaction rate in the temperature range of $0.01T_9$ to $10T_9$ is calculated. We demonstrate that it is possible to correctly convey the available experimental data based on potentials that are consistent with the energies of bound states and their asymptotic constants. For the scattering potentials, we use parameters consistent with the resonance spectrum of the final nucleus.

The results obtained for the reaction rate are approximated by curves of a particular type to simplify their use in applied research. These results apply to problems in nuclear astrophysics related to light atomic nuclei and ultralow energies. The result obtained for the reaction rate is approximated by an analytical expression that can be applied to the problems in nuclear astrophysics related to light atomic nuclei and ultralow energies; for example, in evaluations and calculations of macroscopic characteristics of astrophysics processes like evolution of elements abundances.

This paper is organized as follows. Section II presents the theoretical framework of the MPCM: the classification of cluster states, constructing principles of discrete and continuous states potentials, wave function asymptotics, and cross

*Deceased.

section for the radiative capture processes. Classification of cluster states' and bound states' potentials and the description of the p^6Li channel in the continuous spectrum are given in Secs. III and IV, respectively. Section V is devoted to the astrophysical S factor and the ^{6}Li$(p,\gamma)^7$Be reaction rate. Appendices A and B include the description of the finite-difference method that we are using in the present calculations and a table of numerical values of the p^6Li reaction rate in the temperature range of $0.001T_9$ to $10T_9$, respectively. We outline conclusions in Sec. VI.

II. THEORETICAL FRAMEWORK

Charged-particle-induced reactions represent one of the main inputs in stellar evolution. There are several theoretical models used for description of nuclear reactions at stellar energies that are based on fundamental principles of quantum mechanics. These models and approaches can be generalized as [22] (i) microscopic models where a three- and four-body problem is solved using the exact solution of a few-body system with nucleon-nucleon interactions and the many-body problem is solved by the treatment of all nucleons with exact antisymmetrization of the wave functions and using nucleon-nucleon interactions; (ii) potential models where the nucleon-nucleon interaction is replaced by a nucleus-nucleus force and the unified nucleus is described as a two clusters; (iii) indirect methods when the induced desired reaction is extracted from another reaction; (iv) the R-matrix method. A detailed review of the above mentioned approaches is out of the scope of the present paper. One can find the latest excellent overview in [22] and in references therein.

Since its first application in 1963 [23], the potential model approach has a special place among models for description of low energy reactions. However, over the course of over a half century, this model has been significantly modified and improved. Below we present the fundamentals of the modified potential cluster model, where Young diagrams are used for the classification of orbital states and construction of potentials ([21] and references therein).

The basic framework of the MPCM approach is as follows:

(1) The MPCM is a two-particle model that accounts for the internal characteristics of clusters: their sizes, charges, masses, and quadrupole and magnetic momenta, which are used to calculate the reaction total cross sections or other characteristics of the final nucleus.
(2) The classification of cluster states is performed according to Young's orbital diagrams, leading to the concept of forbidden states in some partial waves [21]. The Pauli principle is implemented via exclusion of the forbidden states (FSs), manifesting in proper node behavior of the radial wave function (WF). Forbidden states that lead to low-lying bound states are not physically realized due to the orthogonality of corresponding functions and allowed state functions.
(3) Gaussian type intercluster interaction potentials are constructed, taking into account these forbidden states in certain partial waves. For each partial wave with specified quantum numbers, the potential is constructed with two parameters, assuming it depends explicitly on Young's orbital diagrams.
(4) Potentials of the bound states (BSs) are constructed based on asymptotic constants (ACs) and binding energies. Potentials of the scattering processes are constructed based on the spectra of the final nucleus or the scattering phase shifts of the particles of the input channel. Parameters of the potentials are fixed or variable within the AC error intervals and vary within the energy or width errors of resonant or excited states.
(5) The radial WFs of the allowed states of the continuous and discrete spectra are tailored appropriately using correct asymptotics.

In light of the new experimental LUNA data [12], we reexamine the ^{6}Li$(p,\gamma)^7$Be reaction S factor and reaction rate within the framework of the MPCM.

A. Classification of cluster states

The total wave functions (WFs) have the form of an antisymmetrized product of completely antisymmetric internal wave functions of clusters $\Psi(1,\ldots,A_1)=\Psi(\mathbf{R_1})$ and $\Psi(A_1+1,\ldots,A)=\Psi(\mathbf{R_2})$, multiplied by the corresponding wave function $\Phi(\mathbf{r})$ of relative motion [24–26]:

$$\Psi=\hat{A}\{\Psi(\mathbf{R_1})\Psi(\mathbf{R_2})\Phi(\mathbf{r})\}. \tag{1}$$

In Eq. (1) $\hat{A}$ is the antisymmetrization operator that permutes nucleons from the clusters A_1 and A_2, $\mathbf{R}_1$ and $\mathbf{R}_2$ are the center-of-mass radius vectors of the clusters, and $\mathbf{r}=\mathbf{R}_1-\mathbf{R}_2$ is the relative motion coordinate.

The wave functions (1) are characterized by specific quantum numbers, including $JLST$—total angular momentum, orbital quantum momentum, spin, and isospin, respectively—and Young's diagrams $\{f\}$, which determine the orbital part of WF permutation symmetry of the relative motion of the clusters.

In the general case, the possible Young's orbital diagram $\{f\}_L$ of some nucleus $A(\{f\})$, consisting of two parts $A_1(\{f_1\})+A_2(\{f_2\})$, is the direct outer product of Young's orbital diagrams $\{f\}_L=\{f_1\}_L\times\{f_2\}_L$ and is determined by Littlewood's theorem. See examples of the application of this theorem in [25,26]. According to Elliott's theorem [27], each Young's diagram is associated with a certain orbital angular momentum or their combination.

Spin-isospin diagrams are the direct inner product of the spin and isospin Young diagrams of a nucleus consisting of A nucleons, $\{f\}_{ST}=\{f\}_S\otimes\{f\}_T$. For a system with no more than eight particles such diagrams are provided in Table C of Ref. [28]. A detailed procedure for defining the corresponding momenta can be found in the classical monograph [29]. Let us note that in Ref. [29] the definition for inner and outer products is reversed.

The total Young's diagram of the nucleus is defined as the direct inner product of the orbital and spin-isospin diagram $\{f\}=\{f\}_L\otimes\{f\}_{ST}$. The total wave function of the system under antisymmetrization does not vanish identically only if

it contains an antisymmetric component $\{1^N\}$, where N is the number of nucleons. In this case the conjugates $\{f\}_L$ and $\{f\}_{ST}$ are multiplied. Therefore, the diagrams $\{f\}_L$ conjugated to $\{f\}_{ST}$ are allowed in this channel. All other orbital symmetries are forbidden since they lead to zero total wave function of the particle system after antisymmetrization.

B. The potentials construction within the MPCM

Let us describe in more detail the procedure for constructing the intercluster partial potentials. Below we define the criteria and outline the sequence for finding parameters for the potentials and indicating their errors as well as ambiguities.

We use a Gaussian potential that depends on the momenta of the system and Young's diagrams:

$$V(r, JLST, \{f_L\}) = -V_0(JLST, \{f_L\}) \exp(-\alpha_{JLST,\{f_L\}} r^2). \tag{2}$$

In Eq. (2) there are two variable parameters: V_0 is the potential depth and α is related to the potential width. The choice of parameters for the bound and scattering states in the p^6Li channel is discussed in detail in Sec. IV.

1. Discrete states

For the bound states of two clusters, the interaction potentials within the framework of the MPCM are constructed based on the requirement imposed to describe the main observable characteristics of such a nucleus. In this case, the potential parameters are fixed. It should be noted that this requirement is an idealized scenario that exists in the nucleus since it assumes that the ground state (GS) is a two-body single channel with probability close to unity. First, we find the parameters of the bound state potentials. For a GS with a given number of bound allowed and forbidden states in the partial wave, these parameters are fixed unambiguously in terms of the binding energy and the AC. When constructing the partial interaction potentials in the MPCM, it is assumed that interactions depend not only on the orbital angular momentum L but also on the total spin S and the total angular momentum J of the system, and also depend on Young's orbital diagrams. As in earlier work [21], we use Gaussian interaction potentials, which depend on the quantum numbers $JLST$, and Young's diagrams $\{f\}_L$. Therefore, for different $JLST$, we have different values of the parameters of the partial potentials.

The accuracy of determining the parameters of the BS potential is connected directly with the accuracy of the AC. The potential does not contain any other ambiguities, since according to Young's diagrams the classification of states makes it possible to unambiguously fix the number of bound forbidden and allowed states in a given partial wave. The number of bound states ultimately determines the depth of the potential, while the width depends entirely on the value of the AC. If one fixes two parameters of the potential using two particular quantities—the binding energy and the AC—the error of the binding energy is seen to be much less than that of the AC.

It should be noted that any calculations of the charge radius reflect the errors of the underlying model. In any model, the magnitude of such a radius depends on the integral of the model wave functions, thereby compounding sources of error. At the same time, the values of ACs are determined from the asymptotic behavior of the model WFs at one point and contain significantly less error. The potentials of the BSs are constructed to obtain the best agreement with the values of the ACs extracted independently from the experimental data. For more details on the general methods of the implementing the asymptotic normalization coefficient (ANC) formalism and its applications; see Ref. [30].

2. Continuum states

For the potentials of the continuous spectrum, the intercluster potential of the nonresonant scattering process for a given number of allowed and forbidden BSs in the considered partial wave is also constructed based on the scattering phase shifts. The accuracy of the potential parameters is associated with the precision of the extracted scattering phase shifts from experimental data. The errors of the extracted phase shifts may be sometimes as high as 20–30%. For the ^{6}Li$(p,\gamma)^7$Be reaction, the potential is unambiguous since the classification, according to Young's diagrams, makes it possible to fix the number of bound states. This completely determines the potential depth, and its width is determined by the shape of the scattering phase shifts.

When constructing the nonresonant scattering potential based on the data for the nuclear spectra, it is difficult to estimate the accuracy of the parameters even for a given number of BSs. However, one can expect that it will not exceed the error discussed above. This potential should lead to a scattering phase shift close to zero or rise to a smoothly decreasing phase shift at low energies, since there are no resonance levels in the spectra of the nucleus.

In resonance scattering, when a relatively narrow resonance is present in the partial wave at low energies for a given number of BSs, the potential is constructed completely unambiguously. The accuracy of determining the parameters of the interaction potentials is determined by the following factors. The depth of the potential depends on the resonance energy E_x and the number of BSs. The width is determined by the accuracy of the experimental values of the level width Γ.

The error of the parameters, approximately 5–10%, usually does not exceed the error of the energy level width. This also applies to the construction of the partial potential from the resonant scattering phase shifts and the determination of its parameters from the spectral resonance of the nucleus [21,31].

C. Wave functions asymptotics

To find radial wave functions of a two-cluster system we solve the radial Schrödinger equation for the central potential:

$$\frac{d^2\chi_{JLST}}{dr^2} + \left[k^2 - V_{\rm nucl}(r) - V_{\rm Coul}(r) - \frac{L(L+1)}{r^2}\right]\chi_{JLST} = 0, \tag{3}$$

where $k = \sqrt{2\mu E}/\hbar$ is the wave number in the center of mass, r is the scalar relative distance between particles in fm, the Coulomb potential $V_{\rm Coul}(r) = 2\mu E/\hbar^2$ has dimension fm^{-2}, $\mu = m_1 m_2/(m_1+m_2)$ is the reduced mass, m_i is the masses of each particle, and $V_{\rm nucl}(r) = 2\mu V(r, JLST)/\hbar^2$.

The case $k^2 > 0$ refers to the continuum. The case $k^2 < 0$ refers to the discrete spectrum and is related to the corresponding channel binding energy E_b, so that $k_0 = \sqrt{2\mu E_b}/\hbar$. See the detailed numerical procedure in Appendix A. To support our framework items 4 and 5 we introduce now the explicit expressions for the corresponding asymptotics of the relative motion wave functions.

The pointlike Coulomb potential is of the form $V_{\rm Coul}(\text{MeV}) = 1.439\,975\,Z_1Z_2/r$, where r is the relative distance between the particles of the channel in fm, and Z_1 and Z_2 are the charges in units of the elementary charge. The Coulomb parameter $\eta = \mu Z_1 Z_2 e^2/k\hbar^2$ is represented in the form $\eta = 3.44476 \times 10^{-2}\, Z_1Z_2\mu/k$.

The discrete solutions of Eq. (3) should fit the proper asymptotics corresponding to the Whittaker equation [32]. In our calculations, the numerical solutions relates to the Whittaker function $W_{-\eta L+1/2}$ via the dimensionless AC denoted as $C_{\rm w}$ [33]

$$\chi_L(r) \underset{r\to R}{\longrightarrow} \sqrt{2k_0}\, C_{\rm w}\, W_{-\eta L+1/2}(2k_0 r). \tag{4}$$

There is another representation for the asymptotics of the bound states wave functions via the dimensional constant C:

$$\chi_L(r) \underset{r\to R}{\longrightarrow} C W_{-\eta L+1/2}(2k_0 r). \tag{5}$$

A dimensional asymptotic constant C is related to the asymptotic normalization coefficient (ANC) A_{NC} by the expression [30]

$$A_{NC} = \sqrt{S_F} C, \tag{6}$$

where S_F is the spectroscopic factor. Further we exploited the constant $C_{\rm w}$ related to ANC as follows:

$$C_{\rm w} = A_{NC}/\sqrt{2k_0 S_F}. \tag{7}$$

In Eqs. (4) and (5) R is the large distance at which the nuclear potential vanishes and $\chi_L(r)$ is the wave function of the bound state obtained from the solution of the radial Schrödinger equation and normalized to unity.

For a continuous spectrum, the function χ_i found numerically is matched to asymptotics $u_L(R)$ of the form

$$N_L u_L(r) \underset{r\to R}{\longrightarrow} F_L(kr) + \tan\left(\delta^J_{S,L}\right) G_L(kr). \tag{8}$$

Here F_L and G_L are Coulomb regular and irregular functions [32]. They are the solutions of the Schrödinger equation with the Coulomb potential. $\delta^J_{S,L}$ are the scattering phase shifts depending on the JLS momenta of the system and N_L is the normalizing constant of the numerical radial function $u_L(R)$ for the continuum.

D. Radiative capture total cross section

To calculate the total cross sections of radiative capture processes, we use the well-known formula for the transitions of NJ multipolarity [21,31],

$$\sigma(NJ, J_f) = \frac{8\pi K e^2}{\hbar^2\, k^3} \frac{\mu}{(2S_1+1)(2S_2+1)} \frac{J+1}{J[(2J+1)!!]^2} \times A^2_J(NJ, K) \sum_{L_i, J_i} P^2_J(NJ, J_f, J_i) I^2_J(k, J_f, J_i) \tag{9}$$

where the matrix elements of orbital $EJ(L)$ transitions have the form ($S = S_i = S_f$)

$$P^2_J(EJ, J_f, J_i) = \delta_{S_i S_f}[(2J+1)(2L_i+1)(2J_i+1)(2J_f+1)] \times (L_i 0 J 0 | L_f 0)^2 \begin{Bmatrix} L_i & S & J_i \\ J_f & J & L_f \end{Bmatrix}, \tag{10}$$

$$A_J(EJ, K) = K^J \mu^J \left(\frac{Z_1}{m_1^J} + (-1)^J \frac{Z_2}{m_2^J} \right),$$

$$I_J(k, J_f, J_i) = \langle \chi_f | r^J | \chi_i \rangle, \tag{11}$$

and the matrix elements of the magnetic $M1(S)$ transition are written as ($S = S_i = S_f, L = L_i = L_f$)

$$P^2_1(M1, J_f, J_i) = \delta_{S_i S_f} \delta_{L_i L_f} [S(S+1)(2S+1)(2J_i+1) \times (2J_f+1)] \begin{Bmatrix} S & L & J_i \\ J_f & 1 & S \end{Bmatrix}, \tag{12}$$

$$A_1(M1, K) = \frac{\hbar K}{m_0 c} \sqrt{3} \left(\mu_1 \frac{m_2}{m_1+m_2} - \mu_2 \frac{m_1}{m_1+m_2} \right),$$

$$I_J(k, J_f, J_i) = \langle \chi_f | r^{J-1} | \chi_i \rangle,\ J = 1. \tag{13}$$

In Eqs. (9)–(13) $K = E_\gamma/\hbar c$ is the wave number of the emitted photon with energy E_γ, and m_1, m_2 and μ_1, μ_2 are the masses and magnetic momenta of the clusters, respectively.

In the present calculations for the reaction ^{6}Li$(p,\gamma)^7$Be, $m_1 \equiv m_p = 1.007\,276\,466\,77$ amu, $m_2 \equiv m_{^6\text{Li}} = 6.015\,123\,2$ amu [34,35]; and $\mu_1 \equiv \mu_p = 2.792\,847\mu_0$, $\mu_2 \equiv \mu_{^6\text{Li}} = 0.822\mu_0$ [34,36], where μ_0 is the nuclear magneton, $\hbar^2/m_0 = 41.4686$ MeV fm^2, where $m_0 = 931.494$ MeV is the atomic mass unit (amu).

III. CLUSTER STATES CLASSIFICATION AND THE BS POTENTIALS IN the $p\,^6$Li CHANNEL

Now we apply the basic framework of MPCM presented above to the study of the ^{6}Li$(p,\gamma)^7$Be reaction. Consider the classification of the BSs of the $p\,^6$Li system according to Young's diagrams. We assume the only one Young's orbital diagram {42} for the ^{6}Li nucleus. One can consider also the {411} diagram; however, its contribution is minor [25]. It is believed that the system's potentials are dependent on the diagrams or combinations of these diagrams in various states. Thus, if the orbital diagram {42} allowed in the ^{2}H ^{4}He-cluster channel is accepted for the ^{6}Li nucleus, then the $p\,^6$Li system with spin $S = 1/2$ contains a forbidden level with diagram {52} and orbital momenta of $L = 0, 2$, and the allowed states with configurations {43} for $L = 1, 3$ and {421} for $L = 1, 2$. Hence, the $p\,^6$Li potentials must have a forbidden state related to {52} in the S wave. The allowed bound state corresponds to the P wave with the two Young's diagrams {43} and {421}.

TABLE I. The classification of the orbital states of the p^6Li system [16,31]. The following notations are used: S and L are spin and orbital angular momentum of the system, respectively, $\{f\}_S$, $\{f\}_T$, and $\{f\}_{ST}$ for isospin $T = 1/2$, and $\{f\}_L$, are spin, isospin, and spin-isospin, and possible orbital Young's diagrams, and $\{f\}_{\rm AS}$, $\{f\}_{\rm FS}$ are Young's diagrams of allowed and forbidden orbital states.

S	$\{f\}_S$	$\{f\}_T$	$\{f\}_{ST}$	$\{f\}_L$	L	$\{f\}_{\rm AS}$	$\{f\}_{\rm FS}$
1/2	{43}	{43}	{7}+{61}+{52}+{511}+{43}	{52}	0, 2		{52}
			+{421}+{331}+{4111}	{43}	1, 3	{43}	
			+{322}+{3211}+{2221}	{421}	1, 2	{421}	
3/2	{52}	{43}	{61}+{52}+{511}	{52}	0, 2		{52}
			+{43}+2{431}+{331}	{43}	1, 3		{43}
			+{322}+{3211}	{421}	1, 2	{421}	

In the quartet spin channel $S = 3/2$ of the system, only one diagram, {421}, is allowed for $L = 1, 2$ [21]. Since there are two allowed diagrams {43} and {421} in the doublet spin state of the p^6Li system, the scattering states turn out to be mixed in orbital symmetries. At the same time, only one allowed diagram {43} usually corresponds to the doublet ground state of the ^{7}Be nucleus in the p^6Li channel with $J^\pi = 3/2^-$ and $L = 1$.

Here, the p^6Li system is completely analogous to the p^2H channel in the ^{3}He nucleus. In the latter case the doublet state is also mixed according to Young's diagrams {3} and {21} [26]. Therefore, the potentials constructed based on the elastic scattering phase shifts of the p^6Li system or the level spectra of the ^{7}Be nucleus cannot be used to describe the GS of the ^{7}Be nucleus in the p^6Li channel. Pure in orbital symmetry with Young's diagram {43}, the $^2P_{3/2}$ potential of the ground state of ^{7}Be reproduces the binding energy of the GS of the nucleus consistent with the p^6Li system and its asymptotic constant.

The scattering potentials are constructed based on the spectra of the ^{7}Be nucleus from Ref. [35]; it has no major difference from the newer compilation [37].

The orbital state's classification of the p^6Li system is shown in Table I. Let us discuss the construction of the Gaussian potential given by Eq. (2). The choice of parameters V_0 and α for the bound ground and first excited state (FES) in the p^6Li channel of ^{7}Be is based on the present classification of the orbital states, data on the binding energy, and asymptotic normalizing constants. The variation procedure of the potential depth and width continues up to reproducing of the binding energy E_b with the given accuracy (10^{-5} MeV, see Table III). As there are few sets of V_0 and α leading to the same values of E_b, we involve one more criterion to minimize this variety: the asymptotic normalizing coefficient. It should be stressed that $C_{\rm w}$ is neither the varying parameter nor the matching one.

A compilation of the AC data for the ground and first excited states in the p^6Li channel of ^{7}Be is presented in Table II, with $C_{\rm w}^2 = A_{NC}^2/2k_0S_F$. Here $\sqrt{2k_0} = 0.983$ fm$^{-1/2}$ for the GS and $\sqrt{2k_0} = 0.963$ fm$^{-1/2}$ for the FES.

Summarizing the data in Table II, we conclude that all cited data on the AC are overlapped. While constructing the corresponding GS and FES potentials, we used the average values indicated in bold in Table II. Recently, a publication by Kiss *et al.* [14] appeared, and it happened that these latest experimental results turned out to be within the defined intervals for ANC given above.

We use GS and FES in the form of only doublet $^2P_{3/2}$ and $^2P_{1/2}$ states, but we take the experimental data on ANC from [40] since it is assumed that these states result in the observed ANC values. We do not consider these states as a mix of doublet and quartet states; for instance, $^{2+4}P_{3/2}$, is a prime example, as the quartet channel is not allowed for the orbital Young's diagram {43} in Table I.

All AC values are used here as a framework to obtain the parameters of the p^6Li interaction BSs' potentials. These

TABLE II. AC data for the ground and the first excited states in the p^6Li channel of ^{7}Be.

BS	Reference	A_{NC} (fm$^{-1/2}$)	S_F	$C_{\rm w}$
GS	Nollett and Wiringa [38], 2011	2.85(3)	1	2.90(3)
	Huang *et al.* [4], 2010	2.01	0.66–1	2.28(24)
	Timofeyuk [39], 2013	1.80	0.46–0.87	**2.32(37)**
	Burtebayev *et al.* [40], 2013	1.77(8)	0.55–0.81	**2.23(31)**
	Gnech and Marcucci [20], 2019	2.654	1.003	2.65
	Kiss *et al.* [14], 2021	2.19(9)	0.98(30)	2.35(43)
FES	Huang *et al.* [4], 2010	1.91	0.66–1.02	2.20(24)
	Timofeyuk [39], 2013	1.91	0.62–1.21	**2.17(36)**
	Burtebayev *et al.* [40], 2013	1.95(9)	0.85–1.03	**2.10(20)**
	Gnech and Marcucci [20], 2019	2.528	1.131	2.53
	Kiss *et al.* [14], 2021	2.18(6)	1.08(32)	2.26(39)

TABLE III. Parameters of p ^{6}Li system bound state potentials and bound states' characteristics. E_x, E_b, and V_0 are provided in MeV. The $R_{\rm ch}$ and $R_{\rm m}$ are given in fm.

No.	BS	E_x	J^π	E_b	$^{2S+1}L_J$	V_0	α (fm^{-2})	$C_{\rm w}$	$R_{\rm ch}$	$R_{\rm m}$
1	GS	0	$3/2^-$	−5.60580	$^2P_{3/2}$	100.750920	0.25	1.75(1)	2.49	2.51
2	GS	0	$3/2^-$	−5.60580	$^2P_{3/2}$	74.504070	0.17	2.26(1)	2.58	2.58
3	GS	0	$3/2^-$	−5.60580	$^2P_{3/2}$	60.998575	0.13	2.74(1)	2.64	2.61
4	FES	0.4291	$1/2^-$	−5.17670	$^2P_{1/2}$	99.473500	0.25	1.68(1)	2.52	2.54
5	FES	0.4291	$1/2^-$	−5.17670	$^2P_{1/2}$	73.333835	0.17	2.16(1)	2.59	2.59
6	FES	0.4291	$1/2^-$	−5.17670	$^2P_{1/2}$	59.898120	0.13	2.61(1)	2.65	2.62

potentials correspond to the lower, upper, and average values of AC and accurately reproduce the binding energies [35] of the bound states. The parameters of the potentials are presented in Table III.

IV. p ^{6}Li CHANNEL IN THE CONTINUOUS SPECTRUM

The resonance behavior of the scattering wave reveals an energy dependence of the corresponding phase shift, i.e., $\delta(E_{\rm res}) = 90^\circ$ or 270°. Based on the generalized Levinson theorem [41], which accounts for forbidden states, $\delta(0) - \delta(\infty) = \pi(N_{AS} + N_{FS})$, where N_{AS} and N_{FS} are the numbers of allowed and forbidden states in definite wave. The natural condition holds. Note that the FSs in continuum exist as bound ones only; therefore, the potential should be deep enough to comprise them. That is the case of S and D potentials in the $p + ^6$Li scattering channel. In the presence of one bound forbidden state, the S phase shift starts at 180, as shown in Fig. 1. The $^2F_{5/2}$, $^2F_{7/2}$, and $^2P_{3/2}$ phase shifts are shown in Fig. 2. If there are no FSs and resonance behavior, then phase shift is close to zero and the potential depth may be chosen as $V_0 = 0$.

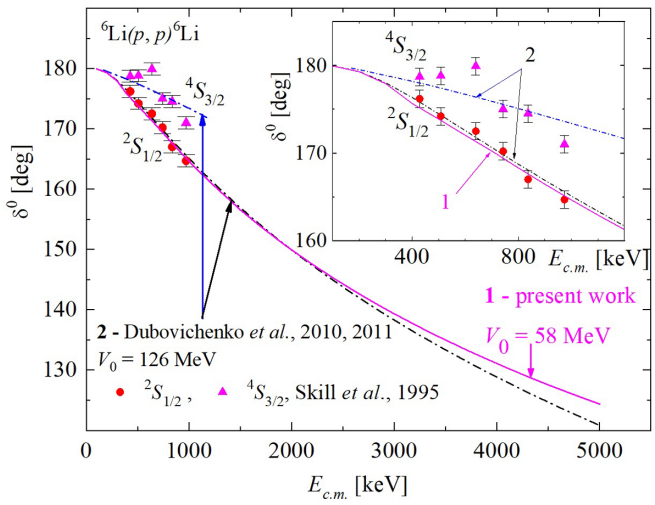

FIG. 1. Doublet and quartet S phase shifts of elastic p ^{6}Li scattering at low energies. The ^2S and ^4S phase shifts are taken from Ref. [42] and shown by ● and ▲, respectively. Results from [16,17] obtained according to [42] are shown by the dashed-dotted curves. Results of the present work are shown by the solid curve.

The parameters of potentials for all scattering processes for transitions to GS and FES are given in Tables IV and V, respectively. In addition, we consider the resonance at an excitation energy of 9.9 MeV [35] according to Fig. 3 (4.3 MeV above the threshold) in a $^2P_{3/2}$ scattering state of width 1.8 MeV in the center of mass. Such an $M1$ transition to the $^2P_{3/2}$ ground state or an $M1$ transition from the $^2P_{1/2}$ scattering state to the $^2P_{1/2}$ FES is possible due to the presence of different Young's diagrams in the bound and scattering states. Recall that the BSs have the diagram {43}, and the scattering states are mixed according to the two diagrams {43} + {421} [17].

Table IV shows possible transitions to the ^{7}Be nucleus GS from various p ^{6}Li scattering states with $^{2S+1}L_J$. The possible transitions to the FES from different scattering states with $^{2S+1}L_J$ are shown in Table V. The resonance energies and widths are obtained with the corresponding parameters of the scattering potentials. For the $P_{1/2}$ scattering wave, zero-depth potentials are used since the scattering P waves do not contain forbidden BSs. For the ^2D wave potentials, ^2S wave parameters are used for $L = 2$.

Resonant phase shifts of elastic scattering $p + ^6$Li are shown in Fig. 2. The above-threshold resonance at 6.73 MeV with a width of 1.2 MeV indicated in Fig. 3 refers to the ^{4}He ^{3}He channel [35] and was not considered in our previous works [16,17]. Note again that, in the MPCM we used,

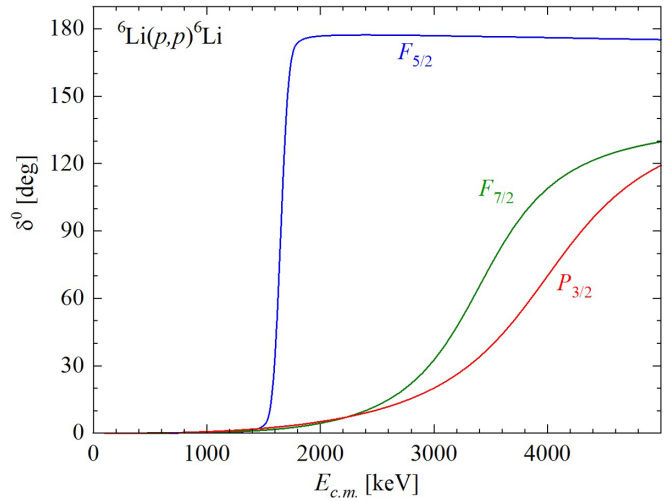

FIG. 2. P and F phase shifts of elastic $p + ^6$Li scattering obtained for scattering potentials with the parameters from Tables IV and V.

TABLE IV. The spectrum of ^{7}Be levels [35] and scattering states in the p^6Li channel for the capture to the $^2P_{3/2}$ GS at a binding energy of 5.6058 MeV, along with P_J^2 from expressions (10) and (12). E_x, $E_{\rm res}$, $\Gamma_{c.m.}$ and V_0 are provided in MeV.

No.	E_x, expt.	J^π	$E_{\rm res}$, expt.	$\Gamma_{c.m.}$, expt.	GS transition: $[^{2S+1}L_J]_i \to [^{2S+1}L_J]_f$	P_J^2	V_0	α, (fm^{-2})	$E_{\rm res}$ theory	$\Gamma_{c.m.}$ theory
1	No res.	$5/2^+$			$E1: {}^2D_{5/2} \to {}^2P_{3/2}$	36/5	58.0	0.4		
2	No res.	$3/2^+$			$E1: {}^2D_{3/2} \to {}^2P_{3/2}$	4/5	58.0	0.4		
3	No res.	$1/2^+$			$E1: {}^2D_{5/2} \to {}^2P_{3/2}$	4	58.0	0.4		
4	No res.	$1/2^-$			$M1: {}^2P_{1/2} \to {}^2P_{3/2}$	4/3	0.0	1.0		
5	7.2(1)	$5/2^-$	1.59(10)	0.40(5)	$E2: {}^2F_{5/2} \to {}^2P_{3/2}$	12/7	111.60	0.1	1.60(1)	0.62(1)
6	9.29(31)	$7/2^-$	3.68(31)	1.93(96)	$E2: {}^2F_{7/2} \to {}^2P_{3/2}$	72/7	44.34	0.05	3.68(1)	1.50(1)
7	9.9	$3/2^-$	4.3	1.8	$M1: {}^2P_{3/2} \to {}^2P_{3/2}$	5/3	432.0	1.5	4.30(1)	1.80(2)

Young's orbital diagram {43} is forbidden in the quartet state, as shown in Table I, and this particular diagram corresponds to the GS of the ^{7}Li nucleus. Therefore, in the GS there is only a doublet $^2P_{3/2}$ state (without impurity of $^4P_{3/2}$), which is allowed for the diagram {43}. Thus, our model [16,17] predicted the absence of resonance at 6.73 MeV with $J^\pi = 5/2$ in the nucleon channel, or, in other words, the impossibility of the $M1$ transition from this resonance to the GS. This has been confirmed by the new LUNA results [12] and, indirectly, by the data of [35]. The width of the resonance peak at 9.29 MeV is taken from Table 7.10 of [35], although another state, $^2P_{1/2}$, is indicated therein. At 9.27 MeV, the given moment is 7/2, as per Table 7.7 in Ref. [35], so we infer the presence of an F state. However, this resonance leads to a minimal increase in cross sections at the $E2$ transition. It is negligible against the background of the $E1$ resonance at 4.3 MeV with a transition from the $^2P_{3/2}$ scattering state for the potential parameters No. 7 (Table IV) or No. 5 (Table V), respectively.

In Fig. 1 are shown the doublet and quartet S phase shifts of elastic p^6Li scattering at low energies. The ^2S potential from Table IV with a depth of 58 MeV has one FS, and allows one to describe the phase shifts of [16] up to 1 MeV, shown in Fig. 1 by solid circles. Moreover, it gives phase shifts below

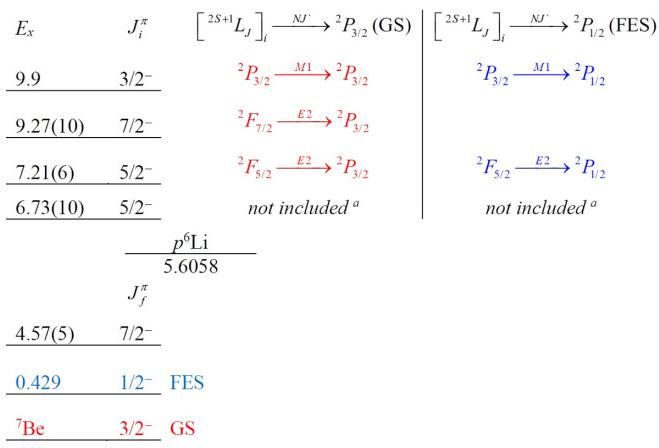

FIG. 3. Schematics of the energy spectrum of ^{7}Be. The energies are given in MeV and the figure is not drawn to scale [35]. Label "[a]" means the above-threshold resonance at 6.73 MeV with a width of 1.2 MeV refers to the ^{4}He ^{3}He channel that is not considered in the present work.

2 MeV that coincide with the phase shifts obtained with the potential from Ref. [16], with a depth of 126 MeV and a width of 0.15 fm^{-2}. This early potential has two FSs and does not agree with our new classification from Table I. To compare the results, we construct a new potential (depth 58 MeV) that gives the most overlap in phase shifts from prior work [16]. The phase shift of the new potential is given in Fig. 1 by a solid curve, while dash-dotted curves refer to results from Ref. [16].

V. ASTROPHYSICAL S FACTOR AND REACTION RATE

A special feature of cross sections of nuclear reactions with charged particles at low and ultralow energies is an extreme reduction by several orders of cross section magnitude due to the decrease in transmission probability through the Coulomb barrier. For practical purposes, the astrophysical S factor is introduced as

$$S(E) = \frac{\sigma(E)}{P(E)}E, \quad P(E) = e^{-2\pi\eta}, \tag{14}$$

where the factor $P(E)$ reflects the permeability of the Coulomb barrier.

Following the excellent book by Iliadis [43], we would like to provide a brief discussion of the use of the S factor in conventional calculation schemes in order to clarify the current approach. The definition of the S factor (14) allows one to write the following expression for the reaction rate:

$$N_A\langle\sigma v\rangle = \left(\frac{8}{\pi\mu}\right)^{1/2} N_A(\kappa T_9)^{-3/2}\int_0^\infty e^{-2\pi\eta}S(E)e^{-E/\kappa T_9}dE. \tag{15}$$

In Eq. (15) κ is the Boltzmann constant and N_A is Avogadro's number. A notable effort has been expended to bring the integral in (15) to analytical form. This is possible only if the expansion of the $S(E)$ factor in the E series, given by

$$S(E) \approx S(0) + S'(0)E + S''E^2, \tag{16}$$

is valid at low energies (cf. Ref. [43], Section 3.2). Expression (16) explains the active interest to determine the value $S(0)$ as a key one for the calculation of the reaction rate in the form of (15) with its further analytical parametrizations.

Usually we need to know the S factor at zero energy, which requires extrapolation of calculations or measurements to $S(0)$. However, calculation procedures become unstable at low and ultralow energy. Our calculation procedure allows

TABLE V. The spectrum of ^{7}Be energy levels [35] and scattering states in the $p\,^6$Li channel for the proton capture to the $^2P_{1/2}$ FES at a binding energy of 5.1767 MeV, along with P_J^2 from expressions (10) and (12). E_x, E_{res}, $\Gamma_{c.m.}$ and V_0 are provided in MeV.

No.	E_x, expt.	J^π	E_{res}, expt.	$\Gamma_{c.m.}$, expt.	FES transition: $[^{2S+1}L_J]_i \to [^{2S+1}L_J]_f$	P_J^2	V_0	α, (fm^{-2})	E_{res} theory	$\Gamma_{c.m.}$ theory
1	No res.	$3/2^+$			$E1:\ ^2D_{3/2} \to\ ^2P_{1/2}$	4	58.0	0.4		
2	No res.	$1/2^+$			$E1:\ ^2S_{1/2} \to\ ^2P_{1/2}$	2	58.0	0.4		
3	No res.	$1/2^-$			$M1:\ ^2P_{1/2} \to\ ^2P_{1/2}$	1/6	0.0	1.0		
4	7.2(1)	$5/2^-$	1.59(10)	0.40(5)	$E2:\ ^2F_{5/2} \to\ ^2P_{1/2}$	6	111.6	0.1	1.60(1)	0.62(1)
5	9.9	$3/2^-$	4.3	1.8	$M1:\ ^2P_{3/2} \to\ ^2P_{1/2}$	4/3	432.0	1.5	4.30(1)	1.80(2)

us obtain a stable solution up to 10 keV that provides more accurate extrapolation. Thus, below we present results for the S factor and reaction rate in the energy range of 10 keV to 5 MeV.

Table VI presents the available experimental data of the astrophysical S factor for the ^{6}Li$(p,\gamma)^7$Be reaction, as well as the extrapolated $S(0)$ values. Results of previous theoretical calculations of the astrophysical S factor of ^{6}Li$(p,\gamma)^7$Be in the framework of different methods [4,14–20,44] and the present work are presented in Table VII. Our calculations are analyzed and interpreted based on the experimental data [12] being among the newest and most accurate.

We studied ^{6}Li$(p,\gamma)^7$Be reaction in [16,17], but limited ourselves to an energy range up to 1 MeV and did not take into account resonances, nor did we consider the reaction rate. In the present work we are including resonances and extending the energy interval for the cross sections and corresponding S factors up to 5 MeV. Moreover, here we present the reaction rate. It is also worth mentioning that in Ref. [20], the authors used the calculation scheme based on [17]. The value $S(0) =$ 95.0 eV b, is obtained, which is consistent with the LUNA experimental data [12]. However, the astrophysical reaction rate is missing in Ref. [20].

The results of the present calculations of S factors along with available experimental data are shown in Figs. 4–6. Figure 4 shows the astrophysical $S(E)$ factor of ^{6}Li$(p,\gamma_0)^7$Be capture to the GS of the ^{7}Be nucleus in an energy range up to 5 MeV. The solid red curve 2 and the two dashed curves, blue 1 and green 3, show the calculation for all transitions to the GS given in Table IV. Parameters V_0 (only integer values) and α of the corresponding potentials as well as C_w from Table III are indicated in the figures, and the parameters of the GS potentials are taken from Table IV. The solid red curve 2 is the result for the potential with the set of parameters No. 2 from Table III, leading to the average value of AC.

In Fig. 5, similar curves show the results for transitions and potentials from Table V to FES. FES potentials have three sets of parameters from Table III. The solid red curve 2 shows the results for capture with set No. 5 from Table III, allowing us to determine the average value of AC. This result is in good agreement with the experimental data [9] presented in Fig. 5. The two dashed curves 1 and 3 almost completely cover the interval or band of cross-section errors of the capture to the FES.

In Fig. 6, similar curves show the astrophysical S factor for the total cross sections corresponding to the transition to GS and FES. The two dashed curves 1 and 3 show the range of S factor values due to ambiguities in the AC of the GS and FES. For the scattering potentials, the parameters from Tables IV and V are used.

The best agreement of the S factor with experimental data is achieved for the values of $C_w = 2.74$ for the GS and $C_w =$ 1.68 for the FES. We recommend these values as the most reliable benchmarks for future experimental studies.

Figure 6 shows that almost all experimental data lie between the solid red curve 2 and the green dashed curve 3. If we use the GS and FES potentials' sets of parameters No. 3 and No. 4 from Table III, the result is shown in Fig. 6 by the black curve 4. In this case the experimental data [12] are reproduced entirely, and the S factor at 10 keV is found to be 101 eV b. For the scattering potentials, the data from Tables IV and V are used.

Due to the uncertainty of the S factor that arises from the uncertainty of the AC, it is desirable to select other options for the potentials of the GS and FES to correctly describe the LUNA data [12]. This can be the subject of future work if

TABLE VI. Experimental data on the astrophysical S factor of ^{6}Li$(p,\gamma)^7$Be. $S(E)$ and $S(0)$ are given in eV b and $S(0)$ are extrapolated values.

E (keV)	$S(E)$	$S(0)$	Reference	Method/project
135	51(15)		Switkowski *et al.* [7], 1979	γ-ray Ge(Li) spectrometers for proton bombarding energies 200–1200 keV
340	43(3)		Ostojić *et al.* [8], 1983	Direct radiative capture
40	65	65	Cecil *et al.* [45], 1992	Thick-target γ-ray-to-charged-particle branching ratio measurements
35	40(14)		Bruss [9], 1993	
		79(18)	Prior *et al.* [13], 2004	Polarized proton beams, TUNL
250	95(10)		He *et al.* [11], 2013	320 keV platform with highly charged ions
60	92(6)	95(9)	Piatti *et al.* [12], 2020	LUNA Collaboration

TABLE VII. Theoretical calculations of the astrophysical S factor of ^{6}Li(p, γ)^{7}Be.

$S(0)$ (eV b)	Reference	Model
106	Barker [44], 1980	Direct-capture potential model
105	Arai *et al.* [15], 2002	Four-cluster microscopic model
95,5	Huang *et al.* [4], 2010	Single-particle model
114	Dubovichenko *et al.* [16,17], 2010, 2011	Modified potential cluster model
73^{+56}_{-11}	Xu *et al.* [18], 2013	Direct-capture potential model
88,34	Dong *et al.* [19], 2017	Gamow shell model
103,9	Gnech and Marcucci [20], 2019	Potential cluster model
$96,5 \pm 5,7$	Kiss *et al.* [14], 2021	Modified two-body potential method
92 ± 12	Kiss *et al.* [14], 2021	Modified two-body potential method
98,3	Present work	Modified potential cluster model

more accurate data are compiled for the AC of the ground and first excited states of the ^{7}Be nucleus.

The approximation of the S factor shown by the black curve 4 in Fig. 6 in the energy range of 30 to 150 keV has an analytical form

$$S(E) = S_0 + S_1E + S_2E^2 \tag{17}$$

with parameters $S_0 = 98.31$ eV b, $S_1 = -187.18$ MeV^{-1}eV b, and $S_2 = 442.51$ MeV^{-2}eV b. This approximation leads to $\chi^2 = 2.4 \times 10^{-4}$. Here and below for the calculation of χ^2, the error for the theoretical data is set to be equal to 5%. This shows that $S(0) = 98.3$ eV b and $S(30) = 93.1$ eV b.

New experimental data from LUNA [12] can be approximated to the first order,

$$S(E) = S_0 + S_1E, \tag{18}$$

with parameters $S_0 = 91.952$ eV b and $S_1 = -75.471$ MeV^{-1} eV b, leading to $\chi^2 = 0.6$ and $S(0) = 92$ eV b.

To compare the calculated S factor at zero energy (10 keV), we present the known results for the total $S(0)$: 79(18) eV b [13], 105 eV b (at 10 keV) [15], and 106 eV b [44]. In [45], the S factor for transitions to the ground state is 39 eV b, for the transition to the first excited state the S factor value is equal to 26 eV b, and the total S factor is 65 eV b. In our previous works [16,17], a value of 114 eV b was obtained. The summary for S factor experimental and theoretical values is presented in Tables VI and VII.

To sum up, our astrophysical S factor is given in Fig. 7 with a solid red curve, together with experimental data and theoretical calculations. The R matrix fit of the data from LUNA Collaboration [12] and Switkowski *et al.* [7] is represented with the solid blue curve. A solid green curve was obtained by Kiss *et al.* [14] using the weighted means of the ANCs from the analysis of the ^{6}Li(^{3}He, d)^{7}Be transfer reaction within the modified two-body potential method (MTBPM). In addition, [14] contains the results for the S factor of the ^{6}Li(p, γ)^{7}Be reaction calculated within the MTBPM, using the values of ANCs obtained from the analysis of the experimental

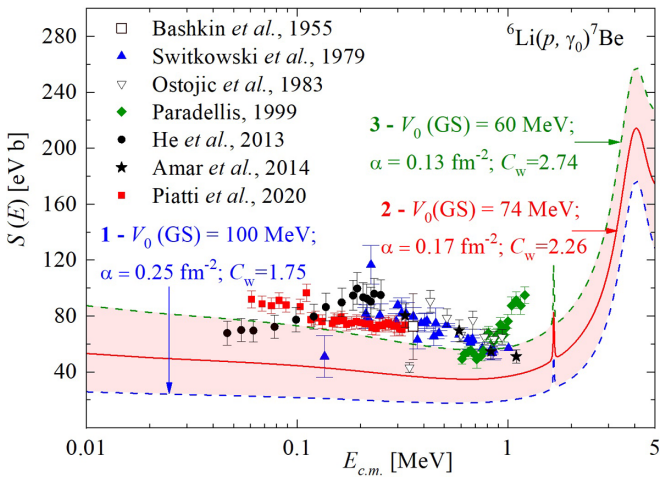

FIG. 4. Astrophysical S factor of the ^{6}Li(p, γ_0)^{7}Be capture to GS. Experimental data are taken from ▲ [7], ● [11], ■ [12], ◆ [10], ⋆ [46], □ [6], ▽ [8]. Parameters of the continuum potential are given in Table IV. A band shows the sensitivity to changes in C_w.

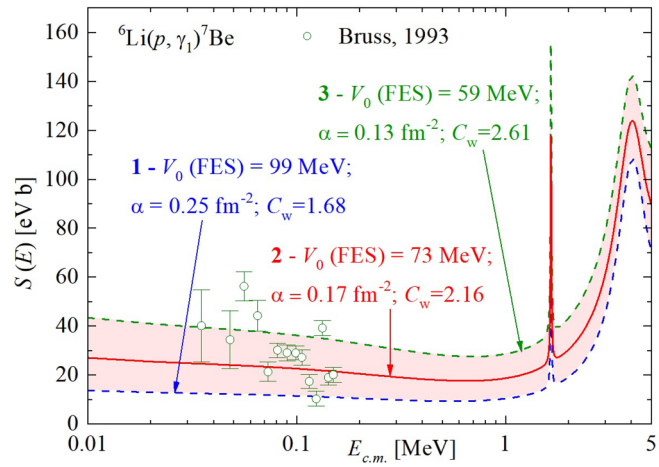

FIG. 5. Astrophysical S factor of the ^{6}Li(p, γ_1)^{7}Be capture to FES. Experimental data ○ are taken from [9]. Parameters of the continuum potential are given in Table V. A band shows the sensitivity to changes in C_w.

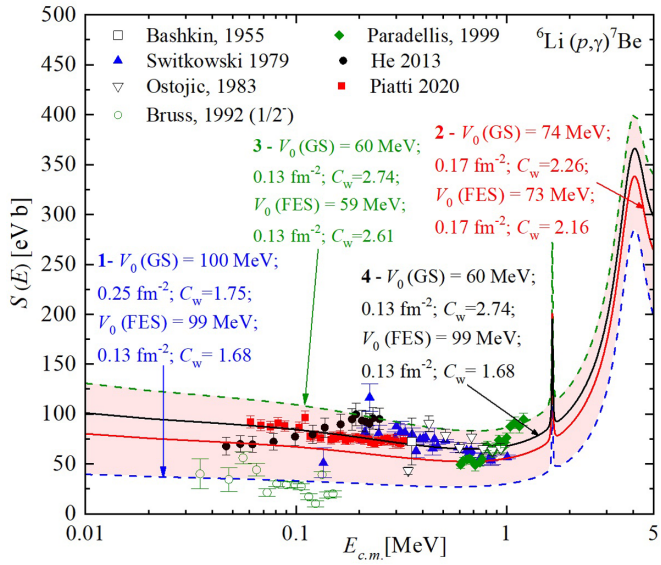

FIG. 6. Astrophysical S factor of the ^{6}Li$(p,\gamma_{0+1})^7$Be capture to GS and FES. Experimental data for capture are from ▲ [7], ● [11], ■ [12], ◆ [10], □ [6], ▽ [8], ⋆ [46], ○ [9]. The parameters of GS and FES potentials are listed in the figure. A band shows the sensitivity to changes in C_w.

astrophysical S factors of the ^{6}Li$(p,\gamma)^7$Be reaction [12]. These results are given in Fig. 7 with the solid black curve.

To calculate the ^{6}Li$(p,\gamma)^7$Be capture reaction rate in units of cm^{3}mol^{-1}s^{-1}, we used an expression [47] analogous to Eq. (15), but substituting the corresponding constant values:

$$N_A\langle\sigma v\rangle = 3.7313\times10^4\,\mu^{-1/2}T_9^{-3/2}\int_0^\infty \sigma(E)E \times \exp(-11.605E/T_9)dE. \quad (19a)$$

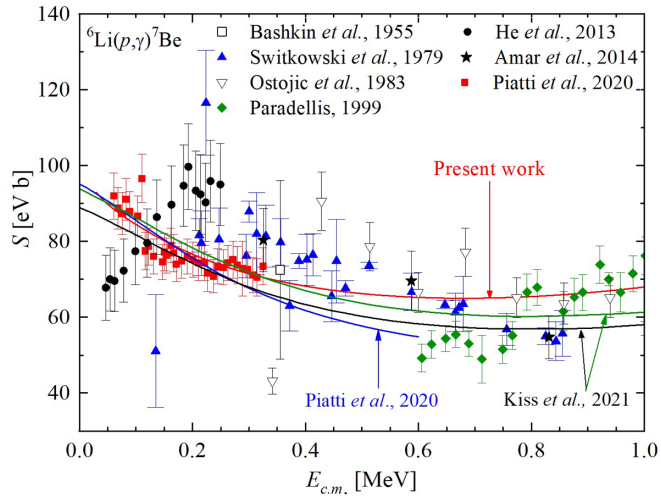

FIG. 7. Comparison of ^{6}Li$(p,\gamma)^7$Be reaction astrophysical S factors. Experimental data for capture to GS and FES are from ▲ [7], ● [11], ■ [12], ◆ [10], □ [6], ▽ [8], ⋆ [46]. Results of calculations: red curve: present work; blue curve: Ref. [12]; black and green curves: Ref. [14].

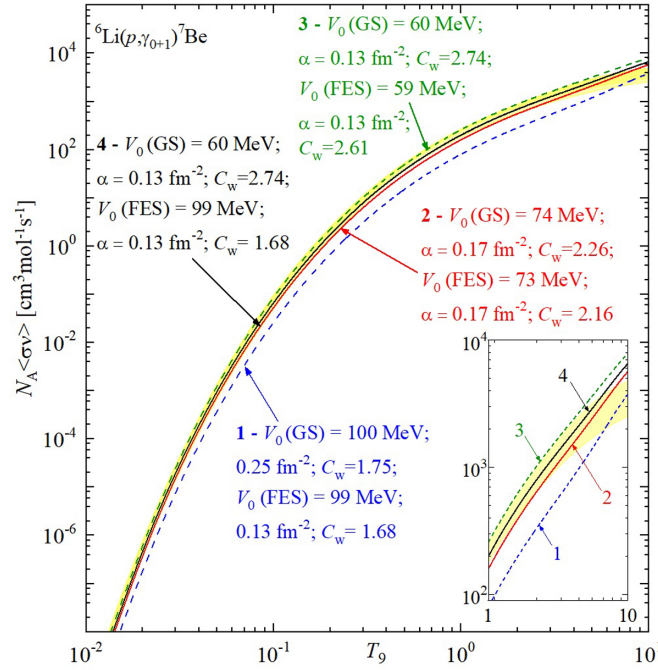

FIG. 8. Total ^{6}Li$(p,\gamma)^7$Be capture reaction rate. Curves indicate the different sums of the capture rates to the GS and FES. Curves are designated as in Fig. 6. The yellow band is taken from Ref. [18].

In Eq. (19) E is given in MeV, the total cross-section $\sigma(E)$ is taken in μb, μ is the reduced mass in amu, and $T_9 = 10^9$ K [47]. Using real integration limits $E_{\min}$ and $E_{\max}$, Eq. (19) becomes

$$N_A\langle\sigma v\rangle = 3.7313\times10^4\,\mu^{-1/2}T_9^{-3/2}\int_{E_{\min}}^{E_{\max}} \sigma(E)E \times \exp(-11.605E/T_9)dE. \quad (19b)$$

It is important to stress this fact as the choice of $E_{\max}$ in Eq. (19b) may have a significant impact on the final result for the reaction rate. The reaction rate (19b) is calculated based on cross-sections, displayed in the form of S factors (14) in Figs. 4–6 within the energy range $E_{\min} = 1$ keV to $E_{\max} = 5$ MeV. The results of these calculations are plotted in Fig. 8.

As noted above, curve 4 in Fig. 6 is in best agreement with all experimental data of the S factor. Therefore, the corresponding reaction rate, also marked as curve 4 in Fig. 7 is the most recommended description of the reaction rate. Curve 4 can be approximated by a function of the form [48]

$$N_A\langle\sigma v\rangle = a_1/T_9^{1/3}\exp\left(-a_2/T_9^{2/3}\right)\left(1 + a_3T_9^{1/3} + a_4T_9^{2/3} + a_5T_9 + a_6T_9^{4/3} + a_7T_9^{5/3}\right) + a_8T_9^{2/3}\exp\left(-a_9/T_9^{1/3}\right). \quad (20)$$

The parameters of approximation (20) with an average value of $\chi^2 = 0.014$ and the error of 5% are given in Table VIII.

Comparing our results with the reaction rates presented in NACRE [47] and NACRE II [18] compilations, we follow the format of Fig. 4 from [12]. We added our results for the

TABLE VIII. The reaction rate approximation parameters.

i	a_i
1	0.00319
2	4.16292
3	3721.884
4	−544516.9
5	16401.8
6	−8044.932
7	85197.34
8	924167.3
9	8.36494

reaction rate, normalized to the reaction rate from NACRE [47]. The comparison is shown in Figs. 9 and 10.

As stated in Ref. [12], the LUNA "thermonuclear reaction rate is 9% lower than NACRE [47] and 33% higher than reported in NACRE II [18] at 2 MK, and the reaction rate uncertainty has been significantly reduced." Figure 9 shows that the deviation between the adopted reaction rate obtained in [12] and the present calculations in the range of $0.01T_9$ to $1T_9$ does not exceed 5%. Therefore, the present calculations confirm the above conclusion by Piatti *et al.* [12].

Figure 10 shows two of our results: the blue curve 1 is the reaction rate calculated on the basis of the total cross sections in the energy range from 1 keV to 5 MeV, and the green one 2 shows the rate at the upper range of the integration limit $E_{\max} = 0.6$ MeV, and this value corresponded to the upper limit of energy in work [12]. The difference between these curves illustrates the importance of the resonance region contribution for the cross sections in the range of 0.6 to 5 MeV at temperatures above $1T_9$.

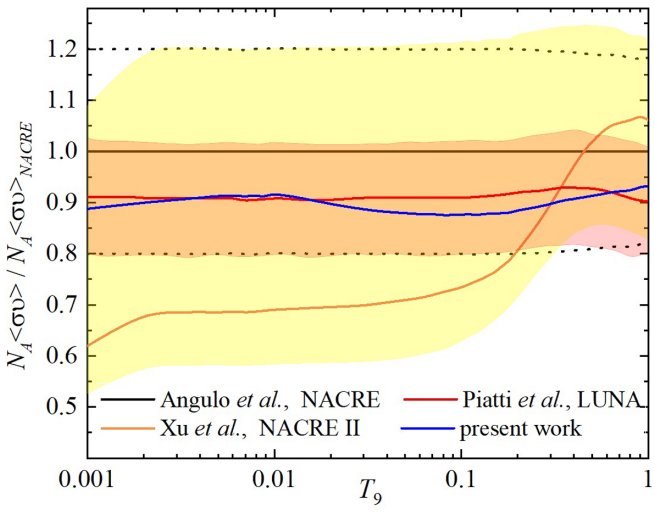

FIG. 9. Comparison of the astrophysical reaction rates in the range $0.001T_9$ to $1T_9$ from [12,18,47] to present work, normalized to the NACRE rate [47]. Dotted curves represent the uncertainty of the NACRE [47] rate, while shaded areas represent the uncertainties from LUNA [12] (pale red) and NACRE II [18] (yellow).

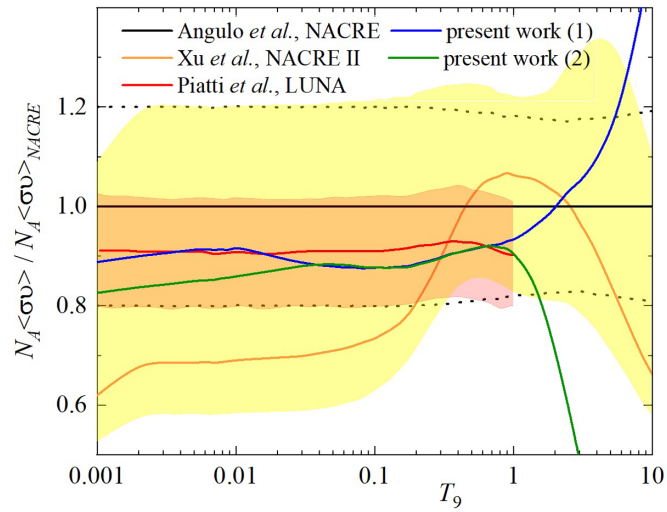

FIG. 10. Comparison of the astrophysical reaction rates in the range $0.001T_9$ to $10T_9$ from [12,18,47] to present work, normalized to the NACRE rate [47]. Dotted curves represent the uncertainty of the NACRE [47] rate, while shaded areas represent the uncertainties from LUNA [12] (pale red) and NACRE II [18] (yellow).

VI. CONCLUSION

We present the results of calculations and analyses of the S factor and astrophysical reaction rate for the ^{6}Li$(p,\gamma)^7$Be reaction in the framework of MPCM. It is demonstrated that the MPCM approach has only one ambiguity arising from the accuracy of the experimentally determined asymptotic constants. This effect manifests as bands in Figs. 4–6 for the astrophysical S factor. Precise LUNA experimental data played a role of the criterion, in reducing the ANC ambiguity with theoretical simulations.

Compared to the R-matrix method, which is constrained by the parametrization of the experimental cross-section data, MPCM enables one to implement calculations in wider energy ranges. We extended the energy interval for the total cross sections and S factors up to 5 MeV, including resonances in the continuum. The numerical signature of this extension is seen in Fig. 10 for the reaction rate.

It was also shown in the present work that MPCM predicted the absence of resonance at 6.73 MeV in the nucleon channel [16,17], which was confirmed by the LUNA results [12], as well as, indirectly, by the data from [35].

We suggest that the NACRE [47] and NACRE II [18] databases should be updated in light of LUNA data [12] and present calculations.

Finally it worthwhile to mention that our theoretical approach for the ^{6}Li$(p,\gamma)^7$Be reaction investigation can be reformulated for the isobar-analog process ^{6}Li$(n,\gamma)^7$Li. The comparative study of these processes within the same theoretical approach can illuminate the lithium cosmological problem. Moreover, our approach allows the investigation of other isobar-analog reactions on nuclei with $A = 5$, 6, and 7 induced by a nucleon capture that lead to the ^{6}Li and ^{7}Li isotopes.

ACKNOWLEDGMENTS

This work was supported by a grant of the Ministry of Education and Science of the Republic of Kazakhstan, No. AP08855556, "Study of additional thermonuclear reactions flowing in the process of controlled thermonuclear fusion on lithium isotopes" through the V. G. Fesenkov Astrophysical Institute of the "National Center of Space Research and Technology" of the Aerospace committee of the Ministry of Digital Development, Innovations and Aerospace Industry of the Republic of Kazakhstan.

APPENDIX A

A solution of a two-body problem for a discrete energy spectrum with a given potential requires finding the binding energy of the system and the wave function of the state. This problem can be solved using the variational method and the finite difference method (FDM) [49]. If both methods are used for the same system of particles, it is possible to control the correctness of the search for the binding energy and WF of the state. We already have used such an approach for p^2H and p^3H systems in [21,50] and demonstrated that the FDM provides a more precise description of the systems. Below we present the FDM approach.

The calculation of the binding energy of a two-cluster system by the FDM relies on the representation of the Schrödinger equation in finite differences [51]. The radial equation for the central potential [49]

$$u_L''(r) + [k^2 - V(r)]u_L(r) = 0 \tag{A1}$$

with some boundary condition for $k^2 < 0$ takes the form of a Sturm-Liouville type boundary value problem. Recasting the second derivative in finite difference form, we obtain

$$u'' = [u_{n+1} - 2u_n + u_{n-1}]/h^2, \quad u_n = u(r_n) \tag{A2}$$

and (A1) becomes a closed system of linear algebraic equations. Thus, for a certain k_0, $D_N(k) = 0$:

$$D_N(k) = \begin{pmatrix} \theta_1 & 1 & 0 & \cdot & \cdot & \cdot & 0 \\ \alpha_2 & \theta_2 & 1 & 0 & \cdot & \cdot & 0 \\ 0 & \alpha_3 & \theta_3 & 1 & 0 & \cdot & 0 \\ \cdot & \cdot & \cdot & \cdot & \cdot & \cdot & \cdot \\ \cdot & \cdot & \cdot & \cdot & \cdot & \cdot & \cdot \\ 0 & \cdot & 0 & 0 & \alpha_{N-1} & \theta_{N-1} & 1 \\ 0 & \cdot & 0 & 0 & 0 & \alpha_N & \theta_N \end{pmatrix} = 0. \tag{A3}$$

Equation (A3) allows one to determine the binding energy E_b of a system of two particles. The elements of the tridiagonal determinant (A3) are defined as follows:

$$\begin{aligned} &\alpha_n = 1, \quad \theta_n = k^2h^2 - 2 - V_nh^2, \quad n = 1, 2, \ldots, N-1, \\ &\alpha_N = 2, \quad \theta_N = k^2h^2 - 2 - V_Nh^2 + 2hf(\eta, L, Z_N), \\ &Z_n = 2kr_n, \quad f(k, \eta, L, Z_n) = -k - \frac{2k\eta}{Z_n} - \frac{2k(L-\eta)}{Z_n^2}. \end{aligned} \tag{A4}$$

Here η is the Coulomb parameter, $k = |\sqrt{k^2}|$ is the wave number expressed in fm^{-1} and determined by the energy of interacting particles in the input channel, and $V_n = V(r_n)$ is the interaction potential of clusters at the point $r_n = nh$ from the interval of zero to R. The number of equations N or the dimension of the determinant usually turns out to be in the range 100 000–1 000 000 [49], $h = \Delta r/N$ is the step of the finite difference grid, and Δr is the solution interval of the system (usually from zero to $r_N = R$).

By writing $f(k, \eta, L, Z_n)$ in the form given in Eq. (A4) it is possible to take the Coulomb interaction into account [32]. The form of the logarithmic derivative of the WF in the external region can be obtained from the integral representation of the Whittaker function [32]

$$f(k, \eta, L, Z) = -k - \frac{2k\eta}{Z} - \frac{2k(L-\eta)}{Z^2}S(\eta, L, Z), \tag{A5}$$

where

$$S(\eta, L, Z) = \frac{\int_0^\infty t^{L+\eta+1}(1 + t/Z)^{L-\eta-1}e^{-t}dt}{\int_0^\infty t^{L+\eta}(1 + t/Z)^{L-\eta}e^{-t}dt}. \tag{A6}$$

Calculations show that the value $S(\eta, L, Z)$ does not exceed 1.05, and its effect on the binding energy of a two-particle system is negligible [49]. When $f(k, 0, 0, Z) = -k$ in Eq. (A5), the binding energy search process is noticeably accelerated.

The calculation of the band determinant $D_N(k)$ for a given k is carried out using recurrent formulas of the form [51]

$$\begin{aligned} &D_{-1} = 0, \quad D_n = \theta_nD_{n-1} - \alpha_nD_{n-2}, \\ &D_0 = 1, \quad n = 1, \ldots, N. \end{aligned} \tag{A7}$$

Any energy E or wave number k that leads to zero determinant

$$D_N(k_0) = 0 \tag{A8}$$

is an eigenenergy of the system E_b or k_0, and the wave function at this energy, determined by recurrent process below, is an eigenfunction of the problem.

Methods for determining the zero of some functional of one variable k are well known [52]. The number N_D of determinant values is determined automatically from the accuracy condition of the binding energy value. The latter one is usually set to the level $\epsilon \approx 10^{-5}$–10^{-9}MeV, and $r_N = R$ is fixed on the range 20–30 fm [49].

After determining the eigenenergy E_b, the WF of this state is sought. To find the shape of the eigenfunctions of bound states, the recurrent procedure

$$\begin{aligned} &u_0 = 0, \quad u_n = \theta_{n-1}u_{n-1} + u_{n-2}, \\ &u_1 = \text{const}, \quad n = 2, \ldots, N. \end{aligned} \tag{A9}$$

is carried out, where u_1 is an arbitrary number, usually fixed on the range 0.01–0.1 [52].

For bound states, the determined WF is normalized to unity. Comparing it to Whittaker asymptotics, one can find an asymptotic constant denoted by C_w (see Sec. II D).

The WF search area R is usually of 20 to 30 fm, and the number of steps N_{WF} for the desired WF is fixed between 10 000 and 50 000. Only in the case of a very low binding energy (0.1–0.2 MeV) is the WF search area increased to 100–200 fm or more.

The recurrence relation (A9) is also used to search for WFs in the case of a continuous spectrum of eigenvalues at

predetermined positive energy ($k^2 > 0$) of interacting particles [49]. However, the WF must now be matched with asymptotics of the form

$$N_L u_L(r) \underset{r\to R}{\longrightarrow} F_L(kr) + \tan\left(\delta^J_{S,L}\right) G_L(kr). \tag{A10}$$

Matching the numerical solution $u_L(R)$ of Eq. (A1) for two points at large distances (R on the order of 10–20 fm) with asymptotics (A10), it is possible to calculate the scattering phase shifts for each value of the momenta JLS for a given energy of interacting particles, as well as the normalization of the WF for scattering processes [49]. To calculate the WF, one can also use the Numerov method [53]. When the number of steps exceeds 10 000, both methods yield the same results within the typical required accuracy. Such results can be compared by calculating the values of AC or charge radii for the BS or the matrix elements for the scattering processes [49].

APPENDIX B

Table IX shows numerical values of the p^6Li reaction rate.

TABLE IX. The astrophysical ^{6}Li$(p,\gamma)^7$Be reaction rate in the range of $0.001T_9$ to $10T_9$.

Temperature (units of T_9)	Reaction rate (cm^{3}mol^{-1}s^{-1})
0.001	3.20×10^{-29}
0.002	7.07×10^{-22}
0.003	2.53×10^{-18}
0.004	4.35×10^{-16}
0.005	1.68×10^{-14}
0.006	2.71×10^{-13}
0.007	2.49×10^{-12}
0.008	1.54×10^{-11}
0.009	7.20×10^{-11}
0.010	2.70×10^{-10}
0.011	8.58×10^{-10}
0.012	2.38×10^{-9}
0.013	5.92×10^{-9}
0.014	1.35×10^{-8}
0.015	2.83×10^{-8}
0.016	5.60×10^{-8}
0.017	1.05×10^{-7}
0.018	1.86×10^{-7}
0.019	3.18×10^{-7}
0.020	5.23×10^{-7}
0.030	1.98×10^{-5}
0.040	1.92×10^{-4}
0.050	9.60×10^{-4}
0.060	3.25×10^{-3}
0.070	8.55×10^{-3}
0.080	1.89×10^{-2}
0.090	3.69×10^{-2}
0.10	6.55×10^{-2}
0.11	1.08×10^{-1}
0.12	1.67×10^{-1}
0.13	2.48×10^{-1}
0.14	3.52×10^{-1}
0.15	4.84×10^{-1}
0.16	6.48×10^{-1}
0.17	8.45×10^{-1}
0.18	1.08×10^{0}
0.19	1.35×10^{0}
0.20	1.67×10^{0}
0.25	3.98×10^{0}
0.30	7.64×10^{0}
0.35	1.28×10^{1}
0.40	1.94×10^{1}
0.45	2.75×10^{1}
0.50	3.71×10^{1}
0.55	4.81×10^{1}
0.60	6.03×10^{1}
0.65	7.37×10^{1}
0.70	8.83×10^{1}
0.75	1.04×10^{2}
0.80	1.20×10^{2}
0.85	1.38×10^{2}
0.90	1.56×10^{2}
0.95	1.74×10^{2}
1.00	1.94×10^{2}
1.25	2.99×10^{2}
1.50	4.13×10^{2}
1.75	5.32×10^{2}
2.00	6.55×10^{2}
2.25	7.80×10^{2}
2.50	9.07×10^{2}
2.75	1.03×10^{3}
3.00	1.16×10^{3}
3.25	1.29×10^{3}
3.50	1.42×10^{3}
3.75	1.56×10^{3}
4.0	1.69×10^{3}
4.5	1.95×10^{3}
5.0	2.22×10^{3}
5.5	2.50×10^{3}
6.0	2.77×10^{3}
6.5	3.05×10^{3}
7.0	3.32×10^{3}
7.5	3.59×10^{3}
8.0	3.86×10^{3}
8.5	4.13×10^{3}
9.0	4.38×10^{3}
9.5	4.63×10^{3}
10	4.88×10^{3}

[1] *Essays in Nuclear Astrophysics: Presented to William A. Fowler, on the Occasion of his Seventieth Birthday*, edited by C. A. Barnes, D. D. Clayton, and D. N. Schramm (Cambridge University Press, New York, 1982), p. 562.

[2] R. N. Boyd, C. R. Brune, G. M. Fuller, and C. J. Smith, Phys. Rev. D **82**, 105005 (2010).

[3] C. Bertulani, J. Phys.: Conf. Ser. **1291**, 012002 (2019).

[4] J. T. Huang, C. A. Bertulani, and V. Guimarães, At. Data Nucl. Data Tables **96**, 824 (2010).

[5] S. Hayakawa, M. L. Cognata, L. Lamia, H. Yamaguchi, D. Kahl, K. Abe, H. Shimizu, L. Yang, O. Beliuskina, S. M. Cha, K. Y. Chae, S. Cherubini, P. Figuera, Z. Ge, M. Gulino, J. Hu, A. Inoue, N. Iwasa, A. Kim, D. Kim *et al.*, Astrophys. J. Lett. **915**, L13 (2021).

[6] S. Bashkin and R. R. Carlson, Phys. Rev. **97**, 1245 (1955).

[7] Z. E. Switkowski, J. C. Heggie, D. L. Kennedy, D. G. Sargood, F. C. Barker, and R. H. Spear, Nucl. Phys. A **331**, 50 (1979).

[8] R. Ostojić, K. Subotić, and B. Stepančić, Nuovo Cimento A **76**, 73 (1983).

[9] R. Bruss, in *Nuclei in the Cosmos: Proceedings of the Second International Symposium on Nuclear Astrophysics*, edited by F. Kappeler and K. Wisshak (IOP, Karlsruhe, 1993), p. 648.

[10] T. Paradellis (unpublished), quoted by [15] as Ref. [25].

[11] J. J. He, S. Z. Chen, C. E. Rolfs, S. W. Xu, J. Hu, X. W. Ma, M. Wiescher, R. J. DeBoer, T. Kajino, M. Kusakabe, L. Y. Zhang, S. Q. Hou, X. Q. Yu, N. T. Zhang, G. Lian, Y. H. Zhang, X. H. Zhou, H. S. Xu, G. Q. Xiao, and W. L. Zhan, Phys. Lett. B **725**, 287 (2013).

[12] D. Piatti, T. Chillery, R. Depalo, M. Aliotta, D. Bemmerer, A. Best, A. Boeltzig, C. Broggini, C. G. Bruno, A. Caciolli, F. Cavanna, G. F. Ciani, P. Corvisiero, L. Csedreki, T. Davinson, A. Di Leva, Z. Elekes, F. Ferraro, E. M. Fiore, A. Formicola *et al.*, Phys. Rev. C **102**, 052802(R) (2020).

[13] R. M. Prior, M. C. Spraker, A. M. Amthor, K. J. Keeter, S. O. Nelson, A. Sabourov, K. Sabourov, A. Tonchev, M. Ahmed, J. H. Kelley, D. R. Tilley, H. R. Weller, and H. M. Hofmann, Phys. Rev. C **70**, 055801 (2004).

[14] G. G. Kiss, M. La Cognata, R. Yarmukhamedov, K. I. Tursunmakhatov, I. Wiedenhöver, L. T. Baby, S. Cherubini, A. Cvetinović, G. D'Agata, P. Figuera, G. L. Guardo, M. Gulino, S. Hayakawa, I. Indelicato, L. Lamia, M. Lattuada, F. Mudò, S. Palmerini, R. G. Pizzone, G. G. Rapisarda *et al.*, Phys. Rev. C **104**, 015807 (2021).

[15] K. Arai, D. Baye, and P. Descouvemont, Nucl. Phys. A **699**, 963 (2002).

[16] S. B. Dubovichenko, N. Burtebaev, D. M. Zazulin, and A. S. Amar, Russ. Phys. J. **53**, 743 (2010).

[17] S. B. Dubovichenko, N. Burtebaev, D. M. Zazulin, Z. K. Kerimkulov, and A. S. Amar, Phys. At. Nucl. **74**, 984 (2011).

[18] Y. Xu, K. Takahashi, S. Goriely, M. Arnould, M. Ohta, and H. Utsunomiya, Nucl. Phys. A **918**, 61 (2013).

[19] G. X. Dong, N. Michel, K. Fossez, M. Płoszajczak, Y. Jaganathen, and R. M. Betan, J. Phys. G: Nucl. Part. Phys. **44**, 045201 (2017).

[20] A. Gnech and L. E. Marcucci, Nucl. Phys. A **987**, 1 (2019).

[21] S. B. Dubovichenko and A. V. Dzhazairov-Kakhramanov, Nucl. Phys. A **941**, 335 (2015).

[22] P. Descouvemont, Front. Astron. Space Sci. **7**, 9 (2020).

[23] T. A. Tombrello and P. D. Parker, Phys. Rev. **131**, 2582 (1963).

[24] K. Wildermuth and Y. C. Tang, *A Unified Theory of the Nucleus* (Vieweg+Teubner Verlag, Wiesbaden, 1977).

[25] V. I. Kukulin, V. G. Neudatchin, I. T. Obukhovski, and Y. F. Smirnov, in *Clusters as Subsystems in Light Nuclei* (Vieweg+Teubner Verlag, Wiesbaden, 1983), pp. 1–155.

[26] V. G. Neudatchin, V. I. Kukulin, V. N. Pomerantsev, and A. A. Sakharuk, Phys. Rev. C **45**, 1512 (1992).

[27] J. Elliott, Proc. R. Soc. London A **245**, 128 (1958).

[28] C. Itzykson and M. Nauenberg, Rev. Mod. Phys. **38**, 95 (1966).

[29] A. Bohr and B. R. Mottelson, in *Nuclear Structure* (World Scientific, Singapore, 1998), pp. 137–307.

[30] A. M. Mukhamedzhanov and R. E. Tribble, Phys. Rev. C **59**, 3418 (1999).

[31] S. B. Dubovichenko, *Thermonuclear Processes in Stars and Universe*, 2nd ed. (Scholar's Press, Saarbrucken, 2015), p. 332.

[32] *Handbook of Mathematical Functions*, edited by M. Abramowitz and I. A. Stegun, 10th ed. (U.S. Government Printing Office, Washington, 1972), p. 1046.

[33] G. R. Plattner and R. D. Viollier, Nucl. Phys. A **365**, 8 (1981).

[34] Physical Measurement Laboratory, https://physics.nist.gov/cgi-bin/cuu/Category?view=html&Atomic+and+nuclear.x=100&Atomic+and+nuclear.y=11.

[35] D. R. Tilley, C. M. Cheves, J. L. Godwin, G. M. Hale, H. M. Hofmann, J. H. Kelley, C. G. Sheu, and H. R. Weller, Nucl. Phys. A **708**, 3 (2002).

[36] V. Varlamov, B. Ishkhanov, and S. Komarov, Atomic Nuclei Map, 2015, http://cdfe.sinp.msu.ru/services/ground/NuclChart_release.html.

[37] S. I. Sukhoruchkin, in *Excited Nuclear States: Supplement to I/25A-F*, edited by H. H. Schopper, Landolt-Börnstein, Group I, Vol. 25G (Springer, Berlin, 2016).

[38] K. M. Nollett and R. B. Wiringa, Phys. Rev. C **83**, 041001 (2011).

[39] N. K. Timofeyuk, Phys. Rev. C **88**, 044315 (2013).

[40] N. Burtebayev, J. Burtebayeva, N. Glushchenko, Z. Kerimkulov, A. Amar, M. Nassurlla, S. Sakuta, S. Artemov, S. Igamov, A. Karakhodzhaev, K. Rusek, and S. Kliczewski, Nucl. Phys. A **909**, 20 (2013).

[41] P. Swan, Proc. R. Soc. London A **228**, 10 (1955).

[42] M. Skill, R. Baumann, G. Keil, N. Kniest, E. Pfaff, M. Preiss, G. Reiter, G. Clausnitzer, M. Haller, and W. Kretschmer, Nucl. Phys. A **581**, 93 (1995).

[43] C. Iliadis, *Nuclear Physics of Stars*, 2nd ed. (Wiley-VCH, Weinheim, 2015), p. 672.

[44] F. Barker, Aust. J. Phys. **33**, 159 (1980).

[45] F. E. Cecil, D. Ferg, H. Liu, J. C. Scorby, J. A. McNeil, and P. D. Kunz, Nucl. Phys. A **539**, 75 (1992).

[46] A. Amar and N. Burtebayev, J. Nucl. Sci. **1**, 15 (2014).

[47] C. Angulo, M. Arnould, M. Rayet, P. Descouvemont, D. Baye, C. Leclercq-Willain, A. Coc, S. Barhoumi, P. Aguer, C. Rolfs, R. Kunz, J. W. Hammer, A. Mayer, T. Paradellis, S. Kossionides, C. Chronidou, K. Spyrou, S. Degl'Innocenti, G. Fiorentini, B. Ricci *et al.*, Nucl. Phys. A **656**, 3 (1999).

[48] G. R. Caughlan and W. A. Fowler, At. Data Nucl. Data Tables **40**, 283 (1988).

[49] S. B. Dubovichenko, *Methods for Calculating Nuclear Characteristics: Nuclear and Thermonuclear Processes*, 2nd ed. (Lambert Academic, Saarbrucken, 2012), p. 425.

[50] S. B. Dubovichenko, A. V. Dzhazairov-Kakhramanov, and N. V. Afanasyeva, Nucl. Phys. A **963**, 52 (2017).

[51] G. Marchuk and V. Kolesov, *Application of Numerical Methods to Neutron Cross-Section Calculations* (Atomizdat, Moscow, 1970), p. 304.

[52] T. Korn and G. A. Korn, *Mathematical Handbook for Scientists and Engineers* (McGraw-Hill, New York, 1968), p. 832.

[53] E. Hairer, S. P. Nørsett, and G. Wanner, *Solving Ordinary Differential Equations I* (Springer-Verlag, Berlin, 1993), p. 528.

Correction: The previously published Figure 5 was a duplicate of Figure 4 and has been replaced with the correct figure.